

The Development of Spatial Attention U-Net for The Recovery of Ionospheric Measurements and The Extraction of Ionospheric Parameters

Guan-Han Huang¹, Alexei V. Dmitriev^{1,2} and Chia-Hsien Lin¹,
Yu-Chi Chang¹, Mon-Chai Hsieh¹, Enkhtuya Tsogtbaatar³,
Merlin M. Mendoza¹, Hao-Wei Hsu¹, Yu-Chiang Lin¹, Lung-Chih Tsai⁴,
Yung-Hui Li⁵

¹Department of Space Science and Engineering, National Central University, Taoyuan City 320317, Taiwan

²Skobeltsyn Institute of Nuclear Physics, Lomonosov Moscow State University, 119899 Moscow, Russia

³Department of Computer Science and Information Engineering, National Central University, Taoyuan City 320317, Taiwan

⁴Center for Space and Remote Sensing Research, National Central University, Taoyuan City 320317, Taiwan

⁵AI Research Center, Hon Hai Research Institute, Taipei 114699, Taiwan

Key Points:

- A deep learning model is applied to the ionogram recovery.
- The model can well identify the combined signals of the sporadic E layer and the ordinary and extraordinary modes of the F2 layer signal.
- Critical frequencies of the modes, and the intersection frequency between them are derived.

arXiv:2209.07581v1 [physics.space-ph] 15 Sep 2022

Abstract

We train a deep learning artificial neural network model, Spatial Attention U-Net to recover useful ionospheric signals from noisy ionogram data measured by Hualien’s Vertical Incidence Pulsed Ionospheric Radar. Our results show that the model can well identify F2 layer ordinary and extraordinary modes (F2o, F2x) and the combined signals of the E layer (ordinary and extraordinary modes and sporadic Es). The model is also capable of identifying some signals that were not labeled. The performance of the model can be significantly degraded by insufficient number of samples in the data set. From the recovered signals, we determine the critical frequencies of F2o and F2x and the intersection frequency between the two signals. The difference between the two critical frequencies is peaking at 0.63 MHz, with the uncertainty being 0.18 MHz.

Plain Language Summary

A large amount of images are retrieved by a specialized instrument designed to make observations in the ionosphere. These images are contaminated by instrumental noises. In order to recover useful signals from these noises, we train a deep learning model. A dataset containing the labeled signals are used for both training and validating the model performance. The desired signals are manually labeled using a labelling software. By comparing the model predictions with the labels, the results show that the model can well-identify the elongated, overlapping, or compact signals. The model is also capable of correcting some missing and incorrect labels. The performance of the model is sensitive to the data number of the corresponding labels fed to the model during training. The recovered useful signals are then used to estimate physical quantities which are important for the study of ionospheric physics.

1 Introduction

The ionosphere is a region of ionized gases, plasmas, populating the upper atmosphere and thermosphere (Kelley, 1989). The ionosphere consists of layers concentrated at specific heights. Radio waves propagate through the ionospheric layers at different group velocities and, hence, split into different wave modes according to the electron density, the magnetic field, etc. An experimental ground-based technique of ionosondes has been used for a long time to investigate the vertical profile of the ionospheric ionization represented by the density of free electrons, so-called electron content (EC).

The data product of ionosonde measurements are ionograms, which exhibit signals deflected by the ionosphere at various virtual heights as a function of the sounding frequency. The virtual height of the deflection is obtained by assuming that the wave beams are propagating at the speed of light. The sounding frequency at which the virtual height rapidly increases is called the critical frequency, which also corresponds to the local maximum of the EC. In addition, the splitting in the sounding frequency between the signals of different wave modes is related to the local magnetic field. These ionogram parameters can be used for the true height analysis (Titheridge, 1988; Tsai et al., 1995), estimating the magnetic field strength (Piggott & Rawer, 1978), and modelling the electron density higher than the deflection height by the Chapman function (X. Huang & Reinisch, 2001). Furthermore, the stability of some ionogram interpretation algorithms (Pulinets, 1995; Hui et al., 2018) rely on the intersection point of the ordinary mode and the extraordinary mode signals.

The ionograms from Hualien’s Vertical Incidence Pulsed Ionospheric Radar (VIPIR) are featured by small and compact signals or thin and elongated signals. These ionograms are contaminated by stripe noises appearing in many frequency bands. Mendoza et al. (2021) showed that the Hualien dataset has stronger noise signals compared with the Jicamarca dataset (Jara & Olivares, 2021).

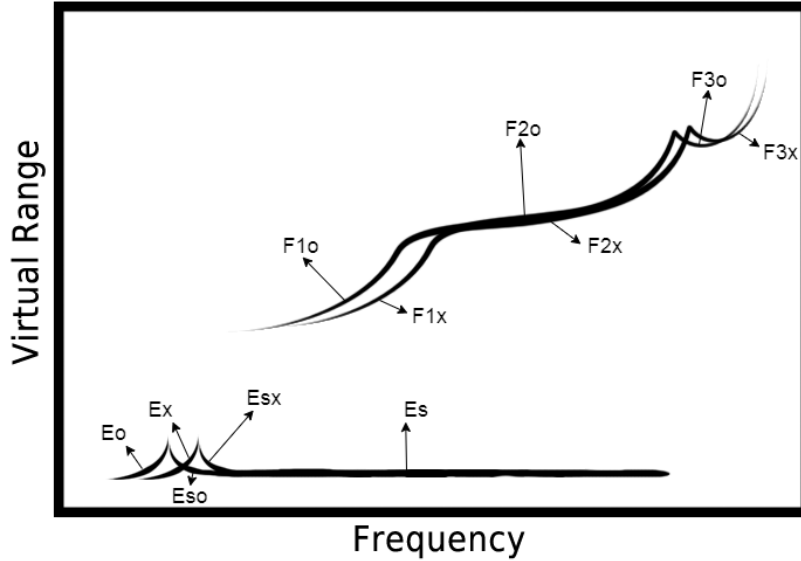


Figure 1. A schematic diagram of ionospheric signals. Different signals are indicated by arrows with annotations (see the text for details).

Thousands of measurements are produced by VIPIR per day. It is hard work and time-consuming for skilled researchers to recover ionospheric signals from such immense dataset. Therefore an automated method based on fuzzy logic (Tsai & Berkey, 2000) has been applied. In recent years, there are also deep learning techniques applied to the ionogram recovery (Mochalov & Mochalova, 2019; Xiao et al., 2020; Jara & Olivares, 2021).

In this research, we implement a deep learning model to the Hualien VIPIR ionograms, and recover different ionogram signals. The data and the preprocessing of the dataset are presented in Section 2. The deep learning model and the validation of the model are described in Section 3. In Section 4, we evaluate the performance of signal recovery (in 4.1), and derive the ionogram parameters from the recovered ionograms (in 4.2). The results are discussed in Section 5 and summarized in Section 6.

2 Data

We use the ionograms acquired from the Hualien VIPIR digisonde operated at Hualien, Taiwan (23.8973°N, 121.5503°E). The dataset contains 6131 ionograms spanning from 2013/11/08 to 2014/06/29. Each ionogram covers a virtual height range up to 800km, and sounding frequency range from 1MHz to 22MHz, and the signal amplitude range up to 100 decibels (dB).

To reduce the data size and remove the calibration signals, we reduce the size of ionograms to virtual height range from 66 to 600km, and sounding frequency from 1.58 to 20.25MHz. Different useful signals in each ionogram are manually identified and labeled into polygons using `labelme` (Wada, 2016). The polygons are rasterized into a binary array of dimension 800x1600x11, which correspond, respectively, to frequency, height and the label. The eleven labels of useful signals are defined as follows (see Figure 1):

1. Eo: Ordinary signal of the E-layer, with the virtual height increasing as the sounding frequency increased.

	Eo	Ex	Esa	F1o	F1x	F2o	F2x
Train (%)	8.13	0.97	52.60	39.22	26.45	94.37	88.10
Validation (%)	8.36	1.33	53.31	38.12	22.53	95.82	87.77
Test (%)	6.77	0.82	52.04	39.97	27.65	94.62	88.34

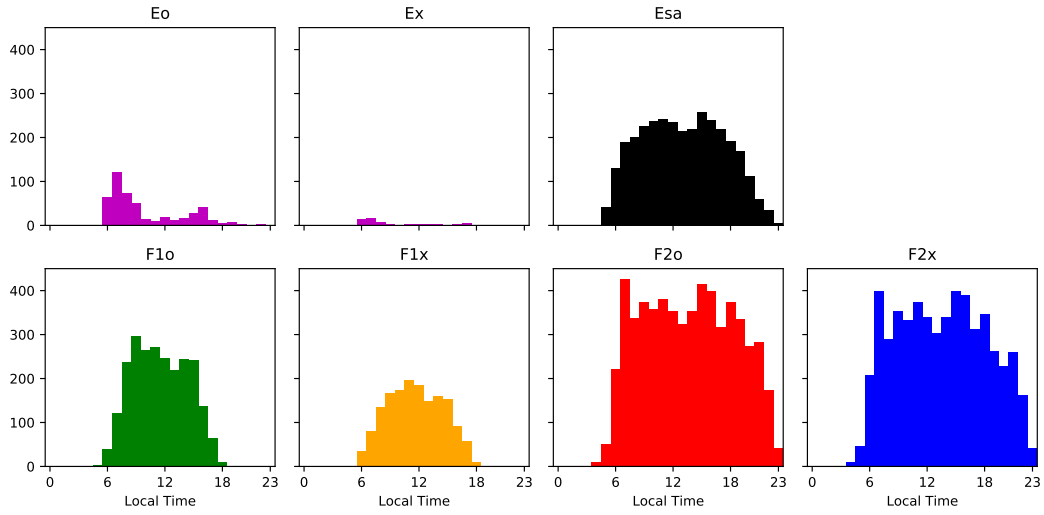
Table 1. Coverage ratio of each signal label in percentage for training, validation and testing set.

2. Ex: Extra-ordinary signal of the E-layer, with the virtual height increasing as the sounding frequency increased.
3. Eso: Ordinary signal of the sporadic E-layer, with the virtual height decreasing as the sounding frequency increased.
4. Esx: Extra-ordinary signal of the sporadic E-layer, with the virtual height decreasing as the sounding frequency increased.
5. Es: Signal of the sporadic E-layer, with the virtual height constant as the sounding frequency increased.
6. F1o: Ordinary signal of the F1-layer, with the virtual height increasing as the sounding frequency increased.
7. F1x: Extra-ordinary signal of the F1-layer, with the virtual height increasing as the sounding frequency increased.
8. F2o: Ordinary signal of the F2-layer.
9. F2x: Extra-ordinary signal of the F2-layer.
10. F3o: Ordinary signal of the F3-layer, with the virtual height increasing as the sounding frequency increased.
11. F3x: Extra-ordinary signal of the F3-layer, with the virtual height increasing as the sounding frequency increased.

The 11 signals shown in Figure 1 usually do not appear simultaneously in all ionograms, and some signals can be too faint to be labeled. The percentages of different labeled signals in our data set are 7.89% for Eo, 0.99% for Ex, 39.81% for Es, 13.34% for Eso, 10.59% for Esx, 39.19% for F1o, 26.06% for F1x, 94.65% for F2o, 88.90% for F2x, 0.13% for F3o and 0.16% for F3x. Eso, Esx, F3o, and F3x have very poor statistics. Therefore, we discarded F3o and F3x to increase the statistics of E layer, and combine Eso, Esx, and Es labels into the Esa label. As a result, we reduce 11 labels into 7 labels. The panels in Figure 2a show the local time distribution of the occurrence of the 7 labels in the bulge of the equatorial ionization anomaly at Taiwan. During the studied time in Taiwan, Esa, F2o, and F2x labels have the highest occurrence rate, and Eo and Ex the lowest. Sporadic Esa and F2 (F2o and F2x) layers occur at all dayside local time hours. F1 layer (F1o and F1x) does not occur in the evening. The E layer (Eo and Ex) occurs mainly in the morning. The panels in Figure 2b show the seasonal distribution of the occurrence of the layers. F2o and F2x as well as F1o and F1x appear in all seasons and have similar distributions. The sporadic layer Esa has the highest occurrence rate during the summer (Shinagawa et al., 2021). Our focus is to recover the Esa, F2o, and F2x labels since the radio wave propagation in the Taiwan region is mostly affected by these layers, due to their high occurrence rate.

Finally, the dataset was split into ratios of 64%, 16% and 20%, respectively, for the training set, the validation set and the test set, resulting in 3925, 981, 1226 ionograms in each set. The coverage ratios of the seven labels in each set are shown in Table 1.

(a) Local time distribution of label occurrence



(b) Seasonal distribution of label occurrence

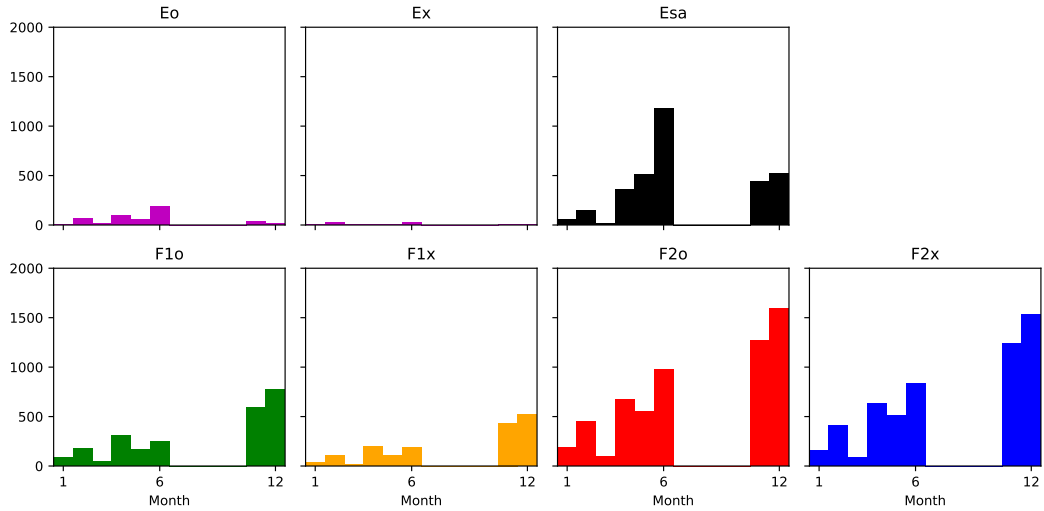


Figure 2. The panels in (a) and in (b) are the local time distributions and seasonal distributions, respectively, of the 7 signal labels, as indicated above the corresponding panels. All panels follow the scale of the left most y-axis.

3 Methodology

3.1 Deep Learning Model

The model employed for this study is Spatial-Attention U-Net (SA-UNet), developed by Guo et al. (2019); Guo et al. (2020). The SA-UNet is featured by a U-Net (Ronneberger et al., 2015) architecture with a spatial attention module at the bottle-neck of the model structure. U-Net has been successful in classifying an image into different labels. With modifications to the U-Net, SA-UNet has been shown that it is capable of identifying vessels from the eyeball images (Guo et al., 2020). The model implementation is also available on Github (<https://github.com/clguo/SA-UNet>). Since vessels and ionogram traces are both tiny or elongated features, we consider that SA-UNet is suitable for the ionogram recovery.

The architecture of the SA-UNet is shown in Figure 3. When an ionogram is sent through the model, the convolution block extracts the features, and the pooling layer reduce the image size. The DropBlock (Ghiasi et al., 2018) randomly drops the image pixels to virtually increase the sample size, which can potentially reduce the overfitting. The spatial attention module rescales the features, so that the model can put more emphasis on important features. The features extracted are assembled and localized in the transpose convolution blocks. The skip-connections return the image size back to the original size. The last convolution layer outputs the probability of the seven signal labels at each pixel. The probability of each label is rounded to a binary value. Since the activation in the last layer is a sigmoid function, which does not normalize the output probability, the model retains the capability of predicting multiple labels for a same pixel. The drop rate of the DropBlock in the original SA-UNet is calculated as follows:

$$\gamma = \frac{1 - P}{K^2} \frac{H}{H - K + 1} \frac{W}{W - K + 1}, \quad (1)$$

where γ is the drop rate, K is the kernel size, H is the height of the image, W is the width of the image, and P is the probability to keep the kernel. To reduce the computational complexity, we slightly modified the above formula of drop rate to the following:

$$\gamma = \frac{1 - P}{K^2}. \quad (2)$$

3.2 Model Training, Evaluation and Optimization

In each training epoch, a mini-batch is fed into the model, and the loss is obtained by calculating the binary crossentropy between the ground truth and the prediction. The model weights are then updated by backpropagating the gradients obtained by the AMS-Grad optimizer (Reddi et al., 2019). An epoch is completed after all mini-batches are used up. The learning rate is set to 0.001 initially, and is halved until it reaches a minimum rate of 10^{-6} if no improvement of the loss of the validation data is found from the previous 5 epochs. A final model is selected from all the epochs by manually checking the performance of the validation set. We found no significant improvement after 60 epochs.

We measure the model performance by the intersection over union (IoU). We modify the definition of IoU in order to apply this to 7 labels. The IoU of each label k in an individual ionogram n , $\text{IoU}_{n,k}$ is computed as the ratio of the total number of intersecting pixels of the ground truth and the prediction ($\text{I}_{n,k} \equiv \text{truth} \cap \text{prediction}$) over the total number of union pixels of ground truth and prediction ($\text{U}_{n,k} \equiv \text{truth} \cup \text{prediction}$). The mean IoU of each label k , IoU_k , is computed as the sum of the intersecting pixels over the sum of the union pixels of all ionograms. The equations for $\text{IoU}_{n,k}$ and mean IoU_k are as follows:

$$\text{IoU}_{n,k} = \frac{\text{I}_{n,k}}{\text{U}_{n,k}}, \quad (3)$$

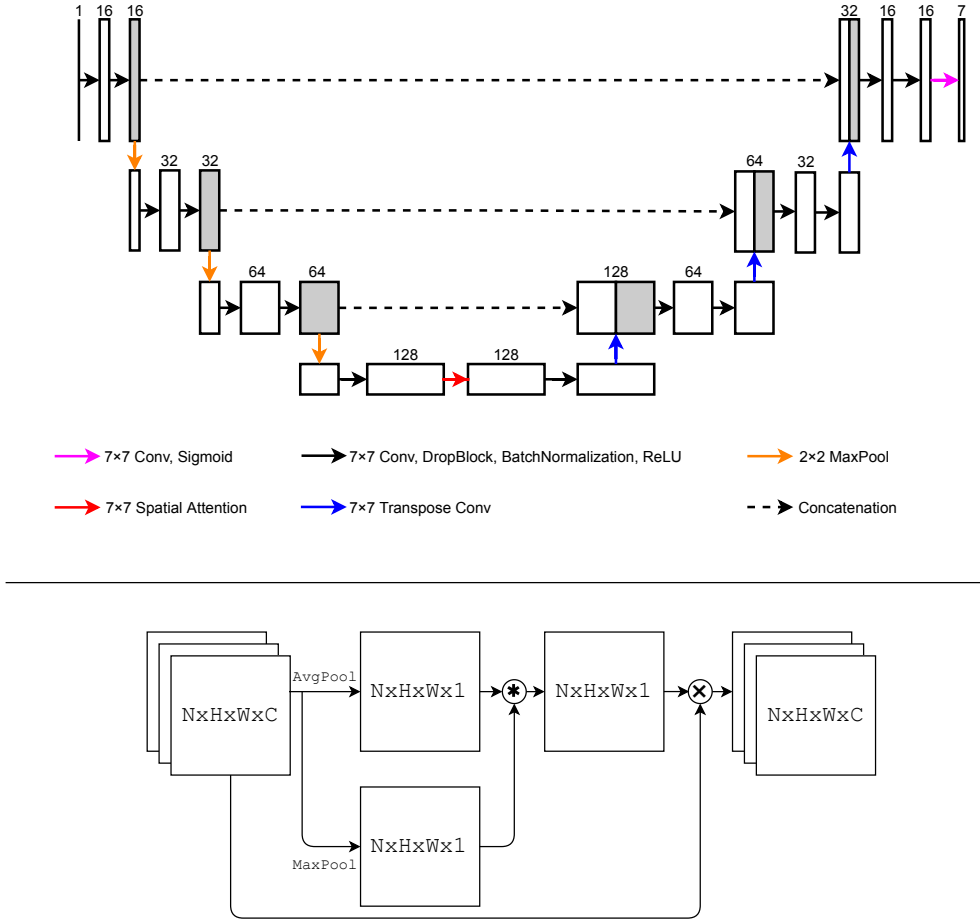


Figure 3. The upper panel shows the architecture of the SA-UNet. The number on top of each rectangle (layer) indicates the dimensionality along the feature space of the input or the output. The lower panel shows the structure of the Spatial Attention module, which is the red arrow in the upper panel. N , H , W , C denote the dimensionality along the sample, height, width, and feature space, respectively. The asterisk and cross signs represent the convolution and the product of array elements, respectively.

	Eo	Ex	Esa	F1o	F1x	F2o	F2x
Test set	83	10	638	490	339	1160	1083
Zero IoUs	52	10	36	114	209	22	88
FN	28	10	14	3	11	3	1
FFP	17	0	9	16	95	9	52
FP	7	0	13	95	103	10	35

Table 2. Rows from top to bottom are the number of instances in the test set, the number of instances with zero IoUs, the number of correctly labeled signals not identified by the model (FN); unlabeled signals correctly identified by the model (FFP); and incorrectly predicted signals (FP).

$$\begin{aligned}
 \text{mean IoU}_k &= \frac{\sum_{n=1}^N U_{n,k} \cdot \text{IoU}_{n,k}}{\sum_{n=1}^N U_{n,k}}, \\
 &= \frac{\sum_{n=1}^N I_{n,k}}{\sum_{n=1}^N U_{n,k}}.
 \end{aligned} \tag{4}$$

The mean IoU is calculated in such a way that we do not encounter zero-division for labels with both $I_{n,k} = 0$ and $U_{n,k} = 0$. An example of application of this technique is shown in Figure 5 (see Section 4.1).

The model is optimized by tuning the hyperparameters. In this study, the hyperparameter includes the size of the convolution kernel, the keep probability of DropBlock, the size of the mini-batch. The default hyperparameters are kernel size of 3×3 , keep probability of 0.85, and batch-size of 4. To prevent a large searching grid, the hyperparameter is tuned individually while the others are fixed to their default values. The size of the convolution kernel varies between 3×3 , 5×5 , and 7×7 ; the keep probability varies between 0.5, 0.7, and 0.85; the size of the mini-batch varies between 1, 2, 4, and 8. This results in 10 different combinations of hyperparameters. By manually comparing the IoUs of the validation data from the 10 combinations of hyperparameters, we determine the optimal hyperparameters as kernel sizes of 7×7 , and the batch size of 4. We found the optimal performance occurs at the 44th epoch.

4 Result

4.1 Recovery of Ionogram Signals

The distribution of IoUs of each label in the test set is plotted in Figure 4 with the mean IoU printed in the corresponding panels. The figure shows that the most accurately recovered signals by SA-UNet are Esa, F2o, and F2x, with mean IoUs reaching approximately 0.7. F1o and F1x are less well recovered, with mean IoU equal to 0.56 and 0.39, respectively. The near-zero mean IoU of Eo and Ex indicates that the model cannot identify these two signals. Comparing the mean IoUs of different labels and their coverage ratio in the training set (Table 1) indicates that the two are highly related: The labels with coverage ratio over 50% are the best recovered labels, and the two labels, Eo and Ex, with the lowest coverage ratios are the worst recovered.

A notable amount of zero IoUs are observed. We divide these zero IoUs into three different types (see Table 2).

1. Model fails to identify correctly labeled signals (false negative, FN): This happens when the model either fails to identify the signal or incorrectly identifies it as other

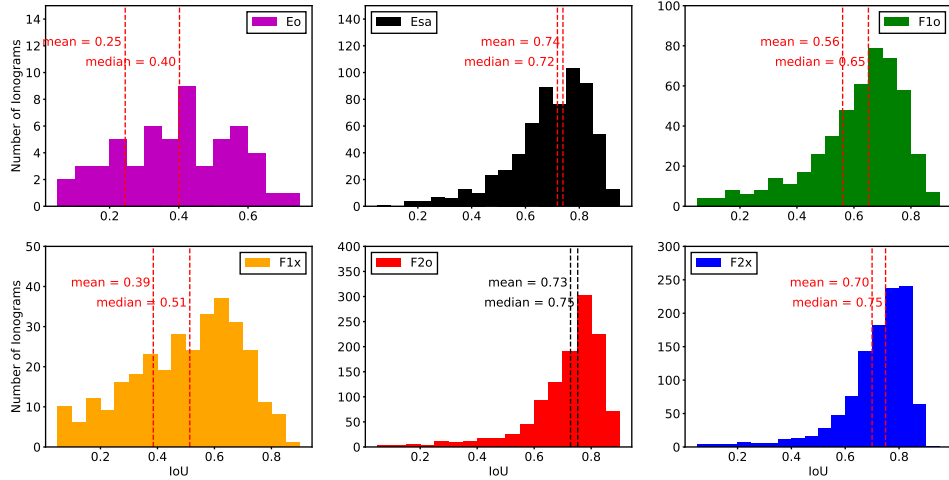


Figure 4. Distribution of non-zero IoU of each label, and the corresponding mean IoU and median IoU. The vertical dashed lines in each panel mark the locations of the mean IoU and median IoU.

- labels. Such situation commonly occurs for the signals with low coverage ratio, which can result in model being undertrained. In fact, all Ex instances in 10 ionograms are identified as Eo label.
2. Model correctly identifies the signals that are not labeled (false false-positive, FFP): This happens when the model correctly identifies the signals that were not labeled or incorrectly labeled. The signals that are overlapping with other signals or are contaminated by strong noise are difficult for human to accurately label them. The correct identification of such signals by our model indicates its superior capability over human eye. One such example can be seen in Figure 5a: there is a tiny Eo signal in the ionogram that was incorrectly labeled as Esa due to strong noise. The model correctly separates the signal into increasing (Eo) and the decreasing (Esa) part, resulting in zero IoU for Eo and lower IoU for Esa.
 3. Model incorrectly identifies the signals that do not exist (false positive; FP): Such situation occurs when the model is overtrained to a specific label, thus trying to identify too many unrelated pixels as the label. For example, in panel (b) of Figure 5, there are only F2o and F2x signals labeled in the ground truth data, but the model divides the beginning parts of F2o and F2x as F1o and F1x signals.

In addition to different types of zero IoUs, mean IoU can also be decreased by echo signals being identified as the primary ones. Echo signals are the signals bouncing between the ground and the ionosphere. In the ionograms, they have similar shapes as the main signals, but appear at higher altitudes with weaker amplitudes. As shown in panel (c) of Figure 5, the model correctly identifies the signals from the ionosonde measurement. However, in panel (d), the echo signals at higher altitude are also identified by the model as F2o and F2x labels, lowering their IoUs as a result.

To investigate the local time and the seasonal dependency of the model performance, we consider the median value of IoU, and use the first and the third quartiles as the error bar. The panels in Figure 6a show the local time variation of IoUs of Eo, Esa, F1o, F1x, F2o, and F2x of the test. Apart from 23:00, the median value of IoU of Esa, F2o, and F2x labels in general are independent of the local time. The panels in Figure 6b show the seasonal variation of the IoUs. The IoUs of F1 (F2o) and F2 (F2o and F2x) layers have a tendency to decrease in the summer, while the IoU of Esa label increases. This

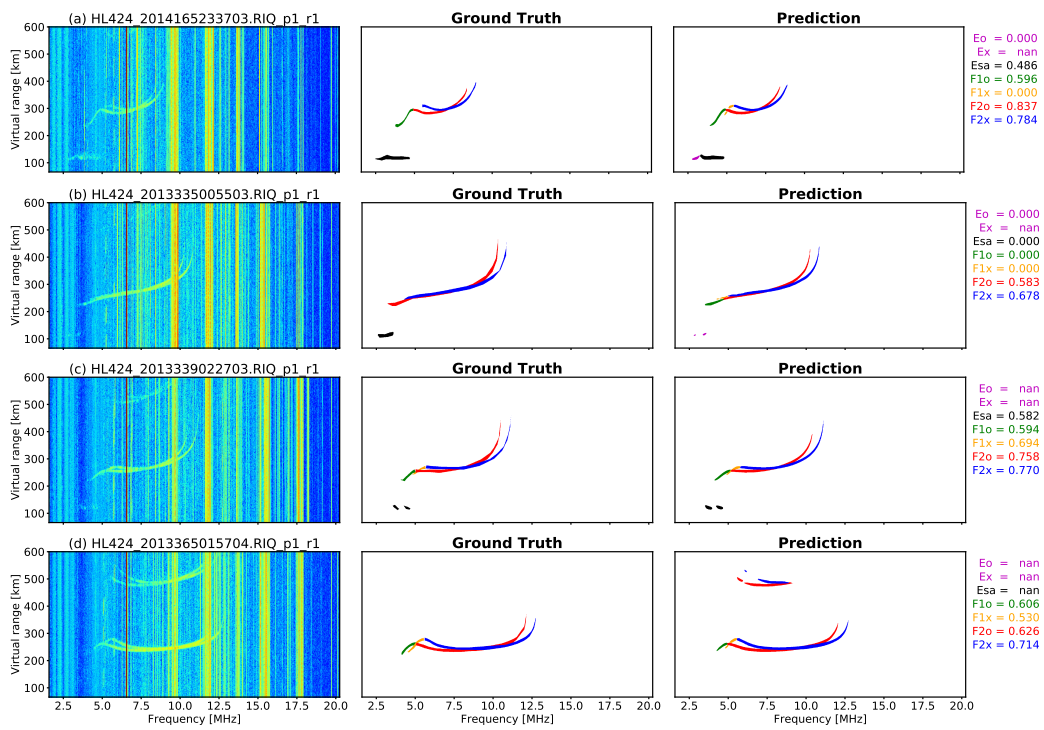


Figure 5. The panels from left to right are the ionograms, their corresponding ground truths, and model predictions. The IoU of each label is printed next to the panels of model prediction. The measurement time of each ionogram: (a) 2014/06/14 23:37:03, (b) 2013/12/01 00:55:03, (c) 2013/12/05 02:27:03, and (d) 2013/12/31 01:57:04.

could be caused by non-uniform statistics of the layers. Namely, sporadic Es has higher occurrence and intensity during summer months. Strong Es layer very often hide the F2 layer such that the statistics of those labels decrease in summer (Mendoza et al., 2021).

4.2 Examination of Ionogram Parameters

From the ionograms recovered by the deep learning model, we extract the virtual heights, the critical frequencies and the intersection frequencies by an automated procedure. In this study, we only present the parameters for F2 signals, because our model performs the best on F2 signals. The same analysis can also be applied to other signals. For a signal $X \in \{\text{F2o}, \text{F2x}\}$ in the n -th recovered ionogram, $X_n(f_i, h'_j)$ at frequency f_i and virtual height h'_j is defined as:

$$X_n(f_i, h'_j) = \begin{cases} 1, & \text{signal of } X; \\ 0, & \text{otherwise.} \end{cases} \quad (5)$$

The virtual height of the F2 signal is defined as the minimum of h'_j where $\text{F2o}(f_i, h'_j)$ is non-zero:

$$h'_{\text{F2}_n} = \min h'_j \text{ of } \text{F2o}_n(f_i, h'_j), \quad (6)$$

$$(7)$$

and the critical frequencies foF2 and fxF2 are defined as the maximum of f_i at which $\text{F2o}(f_i, h'_j)$ and $\text{F2x}(f_i, h'_j)$ are non-zero:

$$\text{foF2}_n = \max f_i \text{ of } \text{F2o}_n(f_i, h'_j), \quad (8)$$

$$\text{fxF2}_n = \max f_i \text{ of } \text{F2x}_n(f_i, h'_j), \quad (9)$$

and the intersection frequency between the F2o and the F2x signals, is defined as the first intersection point from the high frequency.

$$\text{Intersection frequency}(\text{F2o}, \text{F2x}) = \max f_i \text{ of } (\text{F2o}_n \cap \text{F2x}_n) \quad (10)$$

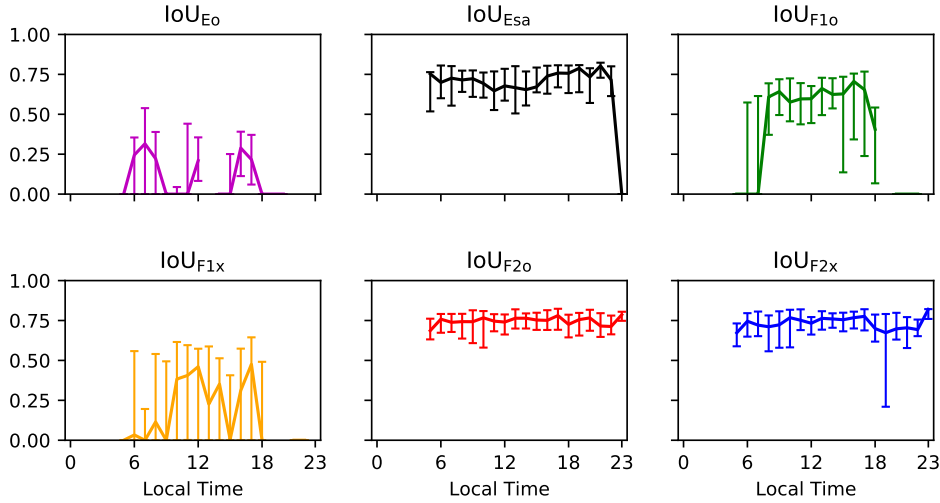
For F2o and F2x signals with large overlapping area, the extracted intersection frequency is not reliable and cannot be used. We consider the overlapping area greater than 0.3 of their combined area as highly overlapped. Out of 1226 ionograms recovered from the test set, 702 are below the threshold. One example is shown in Figure 7a. The corresponding original ionogram is measured at 2013/12/05 02:27:03, the same timestamp as the ionogram in Figure 5c. For this timestamp, the virtual height of F2 is 250.46 km, the critical frequencies foF2 and fxF2 are 10.42 MHz, and 11.14 MHz, respectively, and the intersection frequency between the F2o signal and the F2x signal is 9.25 MHz.

The distributions of foF2 and fxF2 are plotted in Figure 7b. It shows that the extracted foF2 varies from 4.07 MHz to 19.36 MHz. The distribution of the difference between fxF2 and foF2 ($\text{fxF2} - \text{foF2}$) is shown in Figure 7c. It shows a distribution close to a Gaussian profile, with a tail on the left-hand side. The peak of the distribution is 0.63 MHz, and the full-width half-maximum (FWHM) is 0.36 MHz, making the uncertainty of the difference (FWHM/2) to be 0.18 MHz.

5 Discussion

Studies have shown that the deep learning models are able to scale the ionograms automatically. The reported performance of the deep learning models are summarized and compared with our result in Table 3. Jara and Olivares (2021) applied the Autoencoder model (denoted by the superscript a) to extract F region signals from Peru's ionograms, and obtained $\text{IoU} \approx 0.6$ for the combined F layer signals (F1 + F2), after fine-tuning the model parameters. The Fully Convolutional DenseNet model (denoted by the

(a) Local time variation of IoU



(b) Seasonal variation of IoU

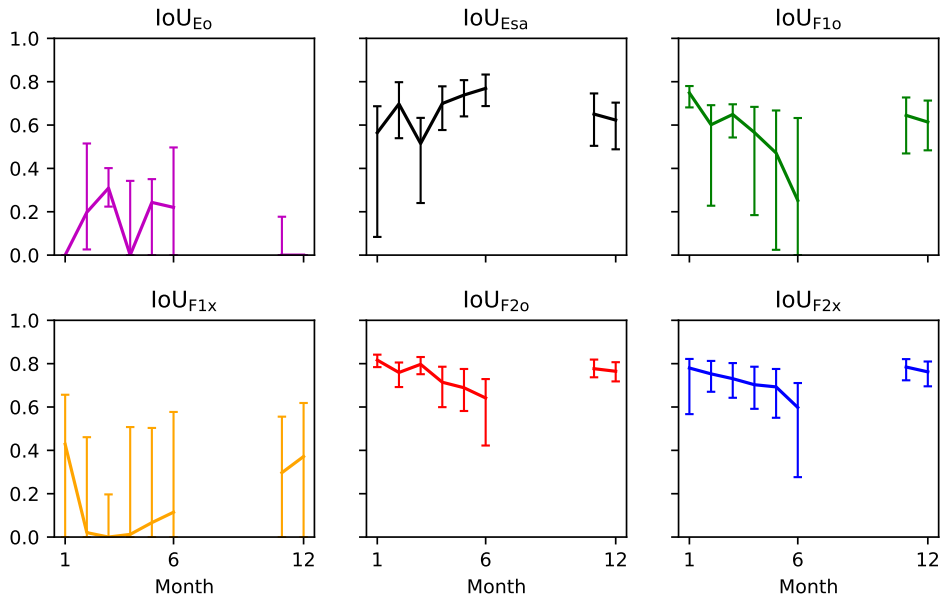


Figure 6. The panels in (a) and in (b) are the local time and seasonal variations of IoUs, respectively, of the 7 signal labels, as indicated above the corresponding panels. All panels follow the scale of the left most y-axis.

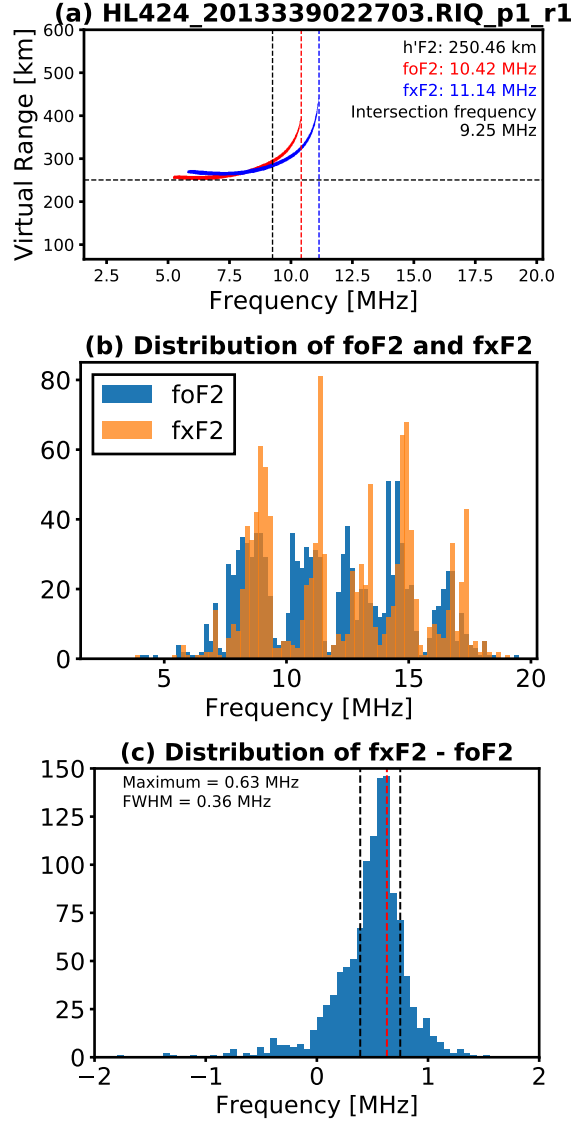


Figure 7. (a) The recovered ionogram at 2013/12/05 02:27:03 showing only F2o and F2x signals. The corresponding critical frequencies of F2o and F2x, and the intersection frequency between the two signals are 10.42 MHz, 11.14 MHz, and 9.25 MHz, respectively, marked by the red, blue, and the black dashed line. (b) The distribution of foF2 (blue bars) and fxF2 (orange bars). (c) The distribution of fxF2 – foF2. Red dashed line indicates the location of the maximum, and black dashed lines indicate the location of the half-maximum.

	Size (HxW)	Metric	Eo	Ex	Esa	F1o	F1x	F2o	F2x
Autoencoder ^a	256x208	IoU	N/A	N/A	N/A			0.60	
FC-DenseNet ^b	800x1600	IoU	0.00	0.00	0.56	0.47	0.33	0.59	0.48
U-Net ^c	64x48	DCL		0.16			0.17		0.11
	192x144	DCL		0.22			0.23		0.19
SA-UNet	800x1600	IoU	0.25	0.00	0.74	0.56	0.39	0.73	0.70
		Recall	0.28	0.00	0.85	0.73	0.51	0.83	0.83
		Precision	0.68	N/A	0.85	0.71	0.61	0.86	0.82
		DCL	0.61	1.00	0.15	0.28	0.44	0.16	0.18

Table 3. The reported performance of different models, and the corresponding size of the input ionograms in units of pixels. DCL denotes the dice-coefficient loss. All metrics are calculated pixel-wise.

superscript b) used in Mendoza et al. (2021) to recover the ionospheric signals obtained an IoU of nearly 0.6 for Esa and F2o layers. Mochalov and Mochalova (2019) used multiple U-Net models (denoted by the superscript c) to scale E, F1, F2 layers, and obtained the dice-coefficient loss (DCL) of 0.16, 0.17, and 0.11 for E, F1 and F2 layers, respectively, in the ionograms of 64x48 pixels, and 0.22, 0.23, and 0.19 in the ionograms of 192x144 pixels. Note that a smaller DCL indicates a better performance. Our SA-UNet model, applied to highly noisy ionograms of 800x1600 pixels, achieves an IoU ≥ 0.7 and DCL score ≤ 0.18 for Esa and F2 layers. To provide additional information for interested readers, we also list the recall rates and precision rates achieved by our model, which are calculated by counting the pixel number of true positives, false positives, and false negatives. It should be noted that the ionograms used by Jara and Olivares (2021) and Mochalov and Mochalova (2019) have been obtained either at middle latitudes or/and in the remote regions with low man-made signals. In short, our study shows that the SA-UNet can improve the performance to IoU ≈ 0.7 and reduce DCL to below 0.18.

The critical frequency foF2 is directly related to the maximum number density N of electrons in F2 layer, and the difference between fxF2 and foF2 can provide an estimation of the local geomagnetic field B (Piggott & Rawer, 1978):

$$N = 1.24 \times 10^{10} \times (\text{foF2}/\text{MHz})^2 [\text{m}^{-3}] \quad (11)$$

$$B \approx 0.71 \times (\text{fxF2} - \text{foF2}) [\text{G}]. \quad (12)$$

Our results show that the derived electron number density ranges from $1.66 \times 10^{11} \text{ m}^{-3}$ to $3.75 \times 10^{12} \text{ m}^{-3}$, and the magnetic field is $B \approx 0.45 \pm 0.13 \text{ G}$. Since the local variation of the geomagnetic field is usually small, the large uncertainty of the magnetic field is likely caused by strong noises in the ionograms. We also find 76 recovered ionograms with foF2 > fxF2. They are caused by both false positive and false negative predictions.

The existence of echoes does not affect the extraction of critical frequencies. However, cares should be taken for extracting the critical virtual heights. In addition to the local geomagnetic field, the difference between foF2 and fxF2 can also be used to estimate foF2 (i.e. foF2 \approx fxF2 - 0.63 MHz) in the case when fxF2 is obtained but F2o cannot be accurately recovered.

The intersection frequency can be used for the verification of the ordinary and extraordinary signals from the F2 layer. Namely, the ascending branch of the ordinary signal should be situated at lower frequencies than the extra-ordinary one. This technique

can provide a robust correction of inaccurate model predictions of the signals from the F2 layer and, thus, more accurate determination of the critical frequencies foF2 and fxF2.

The low percentages of Eo and Ex labels in the training, validation and the test set could bias the model performance. In order to generalize the data representation, an k-fold or a leave-one-out cross validation may be applied (Love et al., 2020; Nishizuka et al., 2021). Moreover, there are a few techniques which may reduce the class imbalance problem, such as undersampling/oversampling to the training set (Lemaître et al., 2017), loss weighted according to the amount of the labels (Raptis et al., 2020; Aminalragia-Giamini et al., 2021), transfer learning from a larger dataset, or ensemble learning of multiple models, to name a few.

It is important to note that the present dataset spans less than one year, and includes only ionospheric statistics at low latitudes under very dynamic region of the bulge of equatorial ionization anomaly. The ionosphere dynamics depends on latitude and varies with solar and geomagnetic activity. Hence, to enable the application of our model to other datasets, the model should be trained on the combination of different data set. Alternatively, the transfer learning technique can be applied to reduce the training time and improve the model performance on a different data set.

6 Conclusions

In this study, we show that SA-UNet is capable of recovering F2o and F2x signals, and the Esa label (which is a combination of Eso, Esx, and Es signals) from the highly contaminated Hualien VIPIR measurements. While the performance of identifying Eo and Ex is poor due to the class imbalance, their low percentage in the statistics suggests that they have little effect on the ionosphere in the Taiwan region. By comparing the input ionogram, ground truth labeling, and the model prediction, our results show that the model is capable of recovering signals that are not labeled, due to contamination by strong noise or overlapping with another signal. The recovered ionograms can be further used in extracting the virtual height, the critical frequency and the intersection frequency of different labels, which are important in the determination of the electron density profile and the magnetic field of the ionosphere overhead.

7 Open Research

The ionogram data and the model used in this study can be openly accessed on Kaggle. The link for the data is provided as follows: <https://www.kaggle.com/changyuchi/ncu-ai-group-data-set-fcdensenet24>. The link for the model is provided as follows: <https://www.kaggle.com/guanhanhuang/ncu-ai> (G.-H. Huang et al., 2022). The model is constructed using Tensorflow 2.3 (Abadi et al., 2015) and its Keras packages, and is trained on Kaggle under the GPU computation environment.

Acknowledgments

This work is funded by the Ministry of Science and Technology of Taiwan under the grant number 109-2923-M-008-001-MY2 and 109-2111-M-008-002. The figures are made by using the Matplotlib package (Hunter, 2007).

References

- Abadi, M., Agarwal, A., Barham, P., Brevdo, E., Chen, Z., Citro, C., . . . Zheng, X. (2015). *TensorFlow: Large-scale machine learning on heterogeneous systems*. Retrieved from <https://tensorflow.org/> (Accessed on 1 June 2022)
- Aminalragia-Giamini, S., Raptis, S., Anastasiadis, A., Tsiganos, A., Sandberg, I., Papaioannou, A., . . . Daglis, I. A. (2021, November). Solar Energetic Particle

- Event occurrence prediction using Solar Flare Soft X-ray measurements and Machine Learning. *Journal of Space Weather and Space Climate*, 11, 59. doi: 10.1051/swsc/2021043
- Ghiasi, G., Lin, T.-Y., & Le, Q. V. (2018). *Dropblock: A regularization method for convolutional networks*. arXiv. Retrieved from <https://arxiv.org/abs/1810.12890> doi: 10.48550/ARXIV.1810.12890
- Guo, C., Szemenyei, M., Pei, Y., Yi, Y., & Zhou, W. (2019). Sd-unet: A structured dropout u-net for retinal vessel segmentation. In *2019 IEEE 19th International Conference on Bioinformatics and Bioengineering (BIBE)* (p. 439-444).
- Guo, C., Szemenyei, M., Yi, Y., Wang, W., Chen, B., & Fan, C. (2020). Sa-unet: Spatial attention u-net for retinal vessel segmentation. *ArXiv, abs/2004.03696*.
- Huang, G.-H., Dmitriev, A. V., Tsai, L.-C., Tsogtbaatar, E., Chang, Y.-C., Hsieh, M.-C., ... Lin, C.-H. (2022). *Sa-unet for the recovery of ionograms*. Kaggle. Retrieved from <https://www.kaggle.com/ds/1933301> (Accessed on 1 June 2022) doi: 10.34740/KAGGLE/DS/1933301
- Huang, X., & Reinisch, B. (2001). Vertical electron content from ionograms in real time. *Radio Science - RADIO SCI*, 36, 335-342. doi: 10.1029/1999RS002409
- Hui, H., Chen, Z., Jiang, C.-H., Yang, G.-B., & Zhao, Z.-Y. (2018). Method for automatic scaling of o wave traces from ionograms. *Progress in Geophysics*, 33, 1351-1357. doi: 10.6038/pg2018BB0355
- Hunter, J. D. (2007). Matplotlib: A 2d graphics environment. *Computing in Science & Engineering*, 9(3), 90-95. doi: 10.1109/MCSE.2007.55
- Jara, C., & Olivares, C. (2021). Ionospheric echo detection in digital ionograms using convolutional neural networks. *Radio Science*, 56. doi: 10.1029/2020RS007258
- Kelley, M. C. (1989). Chapter 1 - introductory and background material. In M. C. Kelley (Ed.), *The earth's ionosphere* (p. 1-22). Academic Press. Retrieved from <https://www.sciencedirect.com/science/article/pii/B978012404013750006X> doi: <https://doi.org/10.1016/B978-0-12-404013-7.50006-X>
- Lemaître, G., Nogueira, F., & Aridas, C. K. (2017, jan). Imbalanced-learn: A python toolbox to tackle the curse of imbalanced datasets in machine learning. *J. Mach. Learn. Res.*, 18(1), 559-563.
- Love, T., Neukirch, T., & Parnell, C. E. (2020, June). Analysing AIA Flare Observations using Convolutional Neural Networks. *Frontiers in Astronomy and Space Sciences*, 7, 34. doi: 10.3389/fspas.2020.00034
- Mendoza, M. M., Chang, Y.-C., Dmitriev, A. V., Lin, C.-H., Tsai, L.-C., Li, Y.-H., ... Tsogtbaatar, E. (2021). Recovery of ionospheric signals using fully convolutional densenet and its challenges. *Sensors*, 21(19). Retrieved from <https://www.mdpi.com/1424-8220/21/19/6482> doi: 10.3390/s21196482
- Mochalov, V., & Mochalova, A. (2019). Extraction of ionosphere parameters in ionograms using deep learning. *E3S Web Conf.*, 127, 01004. doi: 10.1051/e3sconf/201912701004
- Nishizuka, N., Kubo, Y., Sugiura, K., Den, M., & Ishii, M. (2021, December). Operational solar flare prediction model using Deep Flare Net. *Earth, Planets and Space*, 73(1), 64. doi: 10.1186/s40623-021-01381-9
- Piggott, W. R., & Rawer, K. (1978). *U.r.s.i. handbook of ionogram interpretation and reduction* (2nd ed.). Natl. Geophys. Data Cent. Boulder, Colo.: World Data Cent. A for Sol.-Terr. Phys. Retrieved from <https://repository.library.noaa.gov/view/noaa/10404>
- Pulinets, S. A. (1995). Automatic vertical ionogram collection, processing and interpretation. In *Ionosonde network and stations* (p. 37-43). Boulder, Colo.: World Data Cent.
- Raptis, S., Aminalragia-Giamini, S., Karlsson, T., & Lindberg, M. (2020, June).

- Classification of Magnetosheath Jets Using Neural Networks and High Resolution OMNI(HRO) Data. *Frontiers in Astronomy and Space Sciences*, 7, 24. doi: 10.3389/fspas.2020.00024
- Reddi, S. J., Kale, S., & Kumar, S. (2019, 04). *On the convergence of adam and beyond*.
- Ronneberger, O., Fischer, P., & Brox, T. (2015). *U-net: Convolutional networks for biomedical image segmentation*.
- Shinagawa, H., Tao, C., Jin, H., Miyoshi, Y., & Fujiwara, H. (2021, December). Numerical prediction of sporadic E layer occurrence using GAIA. *Earth, Planets and Space*, 73(1), 28. doi: 10.1186/s40623-020-01330-y
- Titheridge, J. E. (1988). The real height analysis of ionograms: A generalized formulation. *Radio Science*, 23(5), 831-849. Retrieved from <https://agupubs.onlinelibrary.wiley.com/doi/abs/10.1029/RS023i005p00831> doi: <https://doi.org/10.1029/RS023i005p00831>
- Tsai, L.-C., & Berkey, F. T. (2000). Ionogram analysis using fuzzy segmentation and connectedness techniques. *Radio Science*, 35(5), 1173-1186. doi: 10.1029/1999RS002170
- Tsai, L.-C., Berkey, F. T., & Stiles, G. S. (1995). The true-height analysis of ionograms using simplified numerical procedures. *Radio Science*, 30(4), 949-959. doi: 10.1029/95RS00936
- Wada, K. (2016). *labelme: Image Polygonal Annotation with Python*. <https://github.com/wkentaro/labelme>.
- Xiao, Z., Wang, J., Li, J., Zhao, B., Hu, L., & Liu, L. (2020). Deep-learning for ionogram automatic scaling. *Advances in Space Research*, 66(4), 942-950. Retrieved from <https://www.sciencedirect.com/science/article/pii/S027311772030332X> doi: <https://doi.org/10.1016/j.asr.2020.05.009>